Quantitative analysis of photoinduced thermal force: Surface and volume responses

Junghoon Jahng [1,*] Bongsu Kim,[2,†] and Eun Seong Lee [1,‡]

[1]*Hyperspectral Nano-imaging Team, Korea Research Institute of Standards and Science (KRISS), Daejeon 34113, Republic of Korea*

[2]*Department of Chemistry, University of California, Irvine, California 92697, USA*

(Received 23 June 2022; revised 27 September 2022; accepted 28 September 2022; published 26 October 2022)

Herein, we provide comprehensive understanding of the photoinduced thermal force between the metal coated tip and organic sample in the context of surface and volume responses where the photoinduced dipole force is typically small enough. Surface response is caused by near-field tip-enhanced thermal expansion, whereas volume response is generated via far-field bulk thermal expansion. In this paper, we quantitatively characterize the two responses, which are mediated via interatomic tip-sample forces in photoinduced force microscopy. The major contributors to the surface sensitivity are the field enhancement at the tip end, the small oscillation of the driving amplitude, and the noncontact/gentle tapping force. Other possible parameters such as the repetition period, and the pulse width of the light source are also discussed. This paper offers insights into the quantitative analysis of surface-sensitive and volume-sensitive spectroscopic nanoimaging, which is of great interest to the scientific community.

DOI: 10.1103/PhysRevB.106.155424

I. INTRODUCTION

Owing to recent developments in energy and semiconductor devices, a comprehensive tool is required to understand chemical reactions at the surface and volume of these devices [1,2]. For example, in an electrochemical battery system, chemical reactions typically occur at the electrode surface [3]; however, in an intercalation battery, an ionic front propagates from the surface into the electrode interior and the reactions occur in the bulk of the electrode [4,5]. Therefore, the monitoring of the chemical reactions in some electrochemical systems requires a spectroscopic tool that can distinguish between surface and volume responses.

Photoinduced force microscopy (PiFM) is an imaging technique that combines the high spatial resolution of atomic force microscopy (AFM) with the spectroscopic sensitivity provided by the optical excitation of a sample [6,7]. PiFM originally considers the photoinduced dipole interaction between the polarizable tip and the sample [8–10]. The interaction is strongly manifested by the multireflection process in highly polarizable systems such as electronic transitions [11] or metal/plasmonic materials (negative permittivity) [12–14]. However, recent studies have claimed that the thermal interaction near the molecular resonance can function as a spectroscopic force at the tip-sample junction, even in noncontact regions [15,16]. The light absorption in the sample increases the temperature of it, which causes thermal expansion. This thermal expansion changes the tip-sample distance and the interatomic force between the tip and sample. This force is exhibited by materials with high thermal properties (a high absorption coefficient, a high thermal expansion coefficient, and a low thermal diffusivity).

There are several claims regarding the origin of surface sensitivity in optomechanical spectroscopic nanoimaging techniques such as the photothermal-induced resonance (PTIR) technique, which is also known as AFM-IR [17]. Tapping-mode/surface-sensitive PTIR [18], which is very similar to heterodyne PiFM, implements high-frequency thermal modulation, which may reduce the total thermal expansion to the sample surface. Further, the optomechanical damping effect, which may result from viscoelastic/adhesion interactions [19] or from tip heating [20] under a high electric field.

Thermal interactions, which are sensitive to both surface (near field) and volume (far field) responses, should be quantitatively analyzed under dynamic tip motion to address the cause of surface sensitivity in PiFM. In this paper, we demonstrate that PiFM can be used to quantitatively characterize surface-sensitive and volume-sensitive thermal responses and that the surface sensitivity of PiFM is caused by tip-enhanced thermal expansion. We identify several key parameters affecting the surface sensitivity by observing the transition from the surface to the volume responses. A rigorous theoretical analysis of thermal expansions at the tip-sample junction under dynamic tip motion is presented herein. Comprehensive experimental findings on polarization, mechanical driving amplitude, and force-distance behavior are also presented.

II. THEORY

When light illuminates the tip-sample junction, there can either (both) exist a photoinduced dipole interaction due to the charge oscillation driven by the optical field or (and) a photoinduced thermal expansion due to light absorption [21]. Each interaction is sensitive to the optical and thermal properties of the material. The photoinduced dipoles in the tip and

*phyjjh@kriss.re.kr

†Present address: Analytical Engineering Group, Samsung Advanced Institute of Technology, Suwon 16678, Republic of Korea.

‡eslee@kriss.re.kr

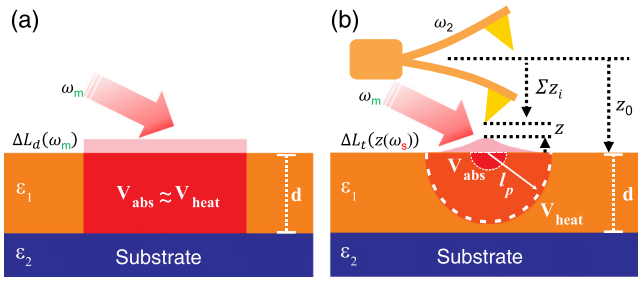

FIG. 1. Schematics of the (a) bulk and (b) tip-enhanced thermal expansions. V_{abs}, V_{heat}, d, l_p, ΔL_b and ΔL_t represent the light absorption volume, sample heating volume, sample thickness, heat-diffusion length at the pulse width (t_p), bulk thermal expansion, and tip-enhanced thermal expansion, respectively. z denotes the instantaneous tip position, z_0 represents the averaged tip-sample distance, and Σz_i denotes the coordinates of the first two eigenmodes, homodyne, and heterodyne motions of the probe.

sample manifest a force through the Coulombic interaction. The typical force range is around a few piconewtons to a few hundreds of piconewtons [22] in highly polarizable materials, such as metal/plasmonic materials, which is two orders of magnitude higher than that in low-polarizable materials, such as most organic polymers.

Conversely, photoinduced thermal expansion is substantially exhibited by materials that effectively confine heat and easily expand thermally, such as organic polymers with a low thermal diffusivity and a high thermal expansion coefficient. The photoinduced thermal expansion can manifest as a force through the tip-sample interatomic force by changing their distance. The photoinduced thermal force (PiTF) for organic polymers near its vibrational resonances typically ranges from a few hundreds of piconewtons to a few tens of nanonewtons [15], which is approximately two to three orders of magnitude higher than that for highly polarizable materials. Therefore, the PiTF for organic polymers usually outweighs its photoinduced dipole force (PiDF) near molecular vibrational resonances [23]. In the next section, we quantitatively discuss the thermal expansions and resulting PiTF for organic polymers with sufficiently small PiDF.

A. Bulk and tip-enhanced thermal expansions

The photoinduced absorption at the pulse width (t_p) depends on the tip-sample geometry, which can be considered involving two cases [15]. The first case is the far-field absorption-based bulk thermal expansion (ΔL_b), which is irrelevant to the tip motion. The other case is the near-field absorption-based tip-enhanced thermal expansion (ΔL_t), which depends on the tip-sample distance. The schematics of both processes are presented in Fig. 1. Thus, the total thermal expansion at t_p may be considered as the sum of both cases, that is, $\Delta L_{tot} = \Delta L_b + \Delta L_t$. In this case, the total thermal expansion can be given as below:

$$\Delta L_{tot}(z) \approx \frac{\sigma l_z \tau_{th}}{\rho C V_{heat}} \int a_{abs} \frac{1}{2} c\varepsilon_0 (|E_f|^2 + |E_n(z')|^2) dV_{abs} \quad (1)$$
$$\equiv \Delta L_b + \Delta L_t(z),$$

with $\tau_{rel} = \frac{4}{\pi^2} \frac{\rho C}{\kappa_{eff}} l_z^2$ and $\tau_{th} = \tau_{rel}(1 - e^{-t_p/\tau_{rel}})$. τ_{rel} is the relaxation (cooling) time, and τ_{th} is the effective thermalization time which considers the heating and cooling time. σ, l_z, ρ, C, and a_{abs} are the linear thermal expansion coefficient, heating length, density, heat capacity, and absorption coefficient of the sample, respectively. z', c, ε_0, E_f, and E_n are the coordinate along the sample thickness, speed of light, vacuum permittivity, far field, and near field inside the sample, respectively. The temperature increase and the resulting thermal expansion were rigorously derived by considering the tip-sample geometries presented in Appendices A and B.

The largest difference between the two thermal expansions is the heating volume (V_{heat}) associated with the absorbing volume (V_{abs}). V_{heat} of the bulk thermal expansion can be assumed as V_{abs} of it, which corresponds to the illuminated IR focal volume. This is because a heat diffusion length (l_p), where $l_p = \sqrt{Dt_p}$ and D is the thermal diffusivity, is typically a few tens of nanometers at a t_p of a few tens of nanoseconds, which is three orders of magnitude smaller than that of the IR focal spot (a few tens of micrometers). Thus, l_z of a thin sample can be directly proportional to the sample thickness (d). Conversely, V_{abs} of the tip-enhanced thermal expansion can be considered the cross section of the tip end and the near-field penetration depth inside the sample. This allows V_{heat} to be limited by the hemispherical thermal diffusion volume at t_p, expressed as $V_{heat} = \frac{2\pi}{3} l_p^3$. In this case, l_z is limited to l_p with increasing sample thickness.

Figure 2 shows the plots of the calculated bulk and tip-enhanced temperature rises (ΔT_b and ΔT_t, respectively) as well as the resulting thermal expansions (i.e, ΔL_b and ΔL_t, respectively) with respect to the thicknesses of exemplar polymer samples [polystyrene (PS), poly(methyl methacrylate) (PMMA), polydimethylsiloxane (PDMS)]. ΔT_b increased as the sample thickness increased to 200 nm, suggesting that the thin samples (<200 nm) cooled rapidly. Afterward, the relaxation time (τ_{rel}) is much longer than the heating time, i.e., t_p, and then the sample heating is saturated with an asymptotically constant temperature rise. This is well explained by the effective thermalization time, $\tau_{th} = \tau_{rel}(1 - e^{-t_p/\tau_{rel}})$, which considers the heating and cooling times (Appendix A). Because V_{abs} of ΔL_b increased while its temperature became saturated with increasing sample thickness, ΔL_b is directly proportional to the sample thickness (the red solid line in the upper panels; Fig. 2).

On the other hand, the thickness dependence of ΔT_t exhibits the peak behavior which is typically caused by the strong tip-enhanced field (heat source) on the higher dielectric substrate such as Si [15]. Since the near-field absorption is saturated owing to the limited absorption volume, the enhanced gap field between the tip and Si substrate leads to the maximum temperature with respect to the polymer thickness. Note that this peak behavior disappears on a low dielectric substrate such as glass [21]. The thickness behavior of ΔL_t is similar to that of the near-field absorption (the red solid line in the lower panels in Fig. 2) due to the limited heating length of ΔL_t. The saturated magnitude of ΔL_t indicates that ΔL_{tot} (blue dashed line) is very similar to ΔL_b with respect to the thickness as shown in the upper panels in Fig. 2.

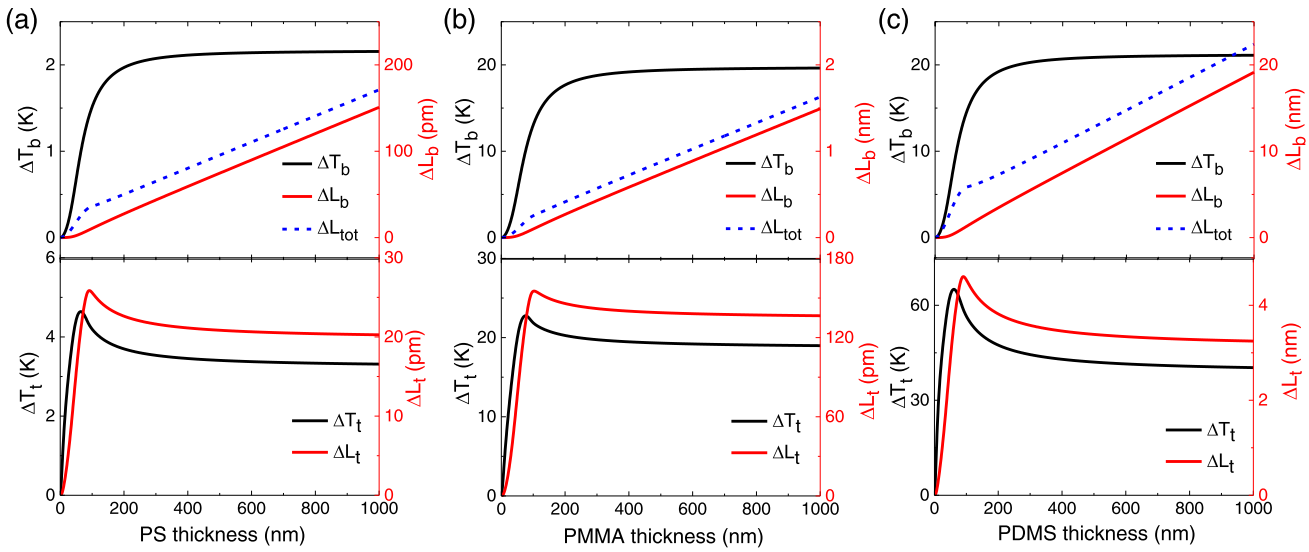

FIG. 2. Calculation of ΔT_t, ΔL_t, ΔT_b, and ΔL_b with respect to the thicknesses of (a) polystyrene (PS), (b) poly(methyl methacrylate) (PMMA), and (c) polydimethylsiloxane (PDMS) polymers on Si substrates at their respective IR absorption resonances. PS, PMMA, and PDMS exhibit the absorption coefficients of $a_{\text{abs}} = 708.47\ \text{cm}^{-1}$ at $1492\ \text{cm}^{-1}$, $a_{\text{abs}} = 8045.61\ \text{cm}^{-1}$ at $1730\ \text{cm}^{-1}$, and $a_{\text{abs}} = 7123.86\ \text{cm}^{-1}$ at $1268\ \text{cm}^{-1}$, respectively [24]. To calculate thermal expansions, we used thermal expansion coefficients and thermal diffusivities of $70 \times 10^{-6}/K$ and $2.5 \times 10^{-7} m^2/s$ for PS, $76 \times 10^{-6}/K$ and $3.0 \times 10^{-7} m^2/s$ for PMMA, and $907 \times 10^{-6}/K$ and $2.6 \times 10^{-7} m^2/s$ for PDMS, respectively [21,25]. The near-field calculation was conducted using the finite dipole method reported in previous studies [25–27]. The blue dashed lines indicate the total thermal expansion, which is the sum of the two thermal expansions (i.e., $\Delta L_{\text{tot}} = \Delta L_b + \Delta L_t$).

The magnitude of thermal expansions depends on the thermal properties of the material. For example, the thermal expansion of PMMA is typically one order of magnitude higher than that of PS, even though σ and D for the polymers are comparable, because the absorption coefficient of PMMA ($a_{\text{abs}} = 8045.61\ \text{cm}^{-1}$) at $1730\ \text{cm}^{-1}$ vibrational resonance [24] is one order of magnitude higher than that of PS ($a_{\text{abs}} = 708.47\ \text{cm}^{-1}$) at $1492\ \text{cm}^{-1}$ vibrational resonance [24]. Additionally, the thermal expansion of PMMA is typically one order of magnitude smaller than that of PDMS, even though they have similar temperature increases due to their similar a_{abs} and D. This is because the linear thermal expansion coefficient of PDMS (907×10^{-6}/K) is one order of magnitude higher than that of PMMA (76×10^{-6}/K) [25].

B. Interatomic tip-sample force change due to thermal expansions

Thermal expansions change the tip-sample distance, which eventually changes the interatomic tip-sample force [16]. The distance-dependent tip-sample force [$F_{\text{ts}}(z)$] can be considered the sum of conservative [$F_{\text{c}}(z)$] and nonconservative [$F_{\text{nc}}(z)$] forces, that is, $F_{\text{ts}}(z) = F_{\text{c}}(z) + F_{\text{nc}}(z)$. The conservative force originates from the distance-dependent potential between the tip and the sample. There are two types of conservative forces at the tip-sample junction. One is the noncontact van der Waals force and the other is the DMT contact force, which are both expressed as

$$F_{\text{c}}(z) \approx \begin{cases} -\frac{H_{\text{eff}}R}{12}\frac{1}{z^2} & (z > r_0) \\ -\frac{H_{\text{eff}}R}{12}\frac{1}{r_0^2} + \frac{4}{3}E^*\sqrt{R}(r_0 - z)^{3/2} & (z < r_0), \end{cases} \quad (2)$$

where H_{eff} is the effective Hamaker constant, R is the tip radius, E^* is the effective Young's modulus, and r_0 is the intermolecular distance, which is around 0.3 nm.

The nonconservative force originates from the dissipation of the oscillator system. The dissipative interaction in the AFM has been typically modeled using a velocity-dependent term, which is expressed as $F_{\text{nc}}(z) = \Gamma(z)\dot{z}$, where $\Gamma(z)$ is the effective damping coefficient for a particular viscoelastic behavior [28]. There can be various forms of $\Gamma(z)$ that describe many physically interesting interactions such as surface energy dissipation [28] and capillary meniscus forces [29]. Additionally, $\Gamma(z)$ has no single explicit form of functions because it depends on each experimental condition. However, it can be reconstructed by solving the inverse problem of probe motion using experimentally accessible quantities such as driving amplitude and phase. The derivation and experimental results are presented in the next section.

To simplify the analytical calculation, only the conservative force was considered. This still maintained the typical behavior of the force-distance curve at the tip-sample junction. Figure 3 depicts plots of the calculated forces between the Au tip and the PS film with respect to the tip-sample distance (blue solid line). The 100 pm thermal expansion of the PS film decreased the tip-sample distance, and the force-distance curve shifted to the right (red dashed line). The variation in the force due to the thermal expansion [i.e., $\Delta F_{\text{ts}}(z) = F_{\text{ts}}(z - \Delta L_{\text{tot}}) - F_{\text{ts}}(z)$] is plotted as a red solid line. Note that the 100 pm thermal expansion can generate additional forces of a few nanonewtons in both the contact (blue-shaded area) and noncontact (red-shaded area) regions. In this manner, the PiTF of the organic monolayer can increase

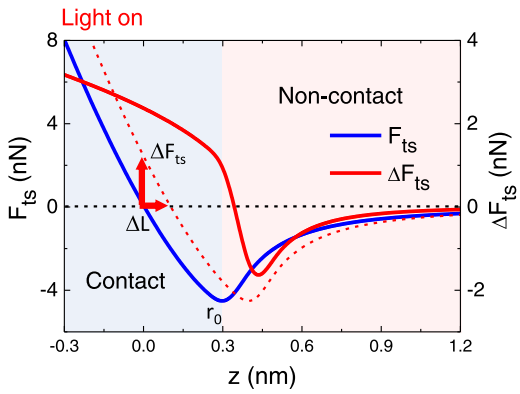

FIG. 3. Calculation of the curve of the force-distance between the Au tip and the PS film with respect to the tip-sample distance z. The red dashed line represents the changed tip-sample force due to the 100 pm thermal expansion. The red solid line represents the difference [i.e., $\Delta F_{ts}(z) = F_{ts}(z - \Delta L_{tot}) - F_{ts}(z)$]. The blue-shaded area represents the repulsive contact region (the negative force gradient) and the red-shaded area represents the attractive noncontact region (the positive force gradient).

to a few hundred piconewtons in the contact region [30], which is a hundred times higher than its PiDF [22].

Since the PiTF is mediated by the interatomic tip-sample force, it also depends on the mechanical properties of the material, such as H_{eff} and E^*. For example, PDMS has a similar H_{eff} to the other polymers such as PS and PMMA, but its E^* (0.6 MPa) is a thousand times lower. Thus, thin PDMS layers under a few nanometers is not very detectable through the repulsive DMT contact force. However, it exhibits a strong signal in the noncontact region via the attractive van der Waals force in a previous study [15].

C. Photoinduced thermal force in dynamic PiFM

Cantilevers are dynamically driven at a frequency (ω_2) and an amplitude (A_2), while the tip-sample junction is illuminated using a laser beam with a modulation frequency (ω_m). If the coordinates of the first two eigenmodes, the homodyne motion at ω_m and heterodyne motion at $\omega_s = \omega_m \pm \omega_2$ are $z_1(t)$, $z_2(t)$, $z_m(t)$, and $z_s(t)$, respectively, then the instantaneous tip position can be expressed as $z(t) \approx z_0 + z_1(t) + z_2(t) + z_m(t) + z_s(t) - \Delta L_{tot}(t)$, where z_0 is the average tip-sample distance. Thus, the time-dependent thermal expansions near the equilibrium position (z_0) under the harmonic approximation may be derived as follows:

$$\Delta L_b(t) \approx \Delta L_b \sin(\omega_m t + \theta_m),$$
$$\Delta L_t(t) \approx \Delta L_t(z_0)\sin(\omega_m t + \theta_m) + \frac{\partial \Delta L_t}{\partial z}|_{z_0} A_2 \sin(\omega_s t + \theta_s), \tag{3}$$

where $\Delta L_{tot}(t) = \Delta L_b(t) + \Delta L_t(t)$, $\omega_s = \omega_m \pm \omega_2$ and $\theta_s = \theta_m \pm \theta_2$. The calculation details lie in Appendix B.

The frequency-dependent force spectrum is generated based on the change in the tip-sample force due to the thermal expansions because the tip oscillates near the sample surface at ω_2. The PiTFs in dynamic tip motion can be obtained using the Taylor expansion of $F_{ts}(z)$ near z_0 as follows:

$$F_{ts}(z) \approx F_c(z_0) + \frac{\partial F_c}{\partial z}(z_1 + z_2) - \Gamma(z_0)(\dot{z}_1 + \dot{z}_2) + F_m + F_s, \tag{4}$$

with

$$|F_m| = \Delta L_{tot}\sqrt{\left(\frac{\partial F_c}{\partial z}\right)^2 + (\Gamma\omega_m)^2}, \tag{5a}$$

$$|F_s| = \frac{A_2}{2}\sqrt{\left(\frac{\partial F_c}{\partial z}\frac{\partial \Delta L_t}{\partial z} + \frac{\partial^2 F_c}{\partial z^2}\Delta L_{tot}\right)^2 + \left(\Gamma\omega_s\frac{\partial \Delta L_t}{\partial z}\right)^2}, \tag{5b}$$

where F_m is the homodyne PiFM force at ω_m and F_s is the heterodyne PiFM force at $\omega_s = \omega_m \pm \omega_2$ (see Appendix B for the calculation details). The physical meaning of Eqs. (5a) and (5b) is that both conservative and nonconservative forces may act as a driving force (gain) when the thermal expansion periodically modulates the tip-sample distance. Note that, the modulated nonconservative force originates from the interatomic tip-sample force rather than the optomechanical damping force [19].

The homodyne PiFM force is directly proportional to the total thermal expansion, but the heterodyne PiFM force is sensitive to the tip-enhanced thermal expansion in the small oscillation limit, where the first derivative term typically dominates the second derivative term. This is the reason why the heterodyne measurement is surface sensitive while the homodyne measurement is volume sensitive. Conversely, the second derivative term can be dominant under a large oscillation in heterodyne PiFM, where the nonlinearity of the tip-sample force increases. This may cause heterodyne PiFM to switch from being surface sensitive to being volume sensitive. This expectation is demonstrated by the experimental results shown in Fig. 5.

The periodic force modulations at ω_m and ω_s can then act as driving forces in the cantilever, the motion of which is demonstrated using the following coupled equations of the driven damped harmonic oscillator system:

$$m\ddot{z}_1 + b_1\dot{z}_1 + k_1 z_1 = F(z), \tag{6}$$

$$m\ddot{z}_2 + b_2\dot{z}_2 + k_2 z_2 = F(z). \tag{7}$$

The total force can be expressed as $F(z) = F_2\sin(\omega_2 t) + F_{ts}(z)$, where F_2 is the constant mechanical driving force. Thereafter, a set of trial solutions, $z_i(t) = A_i\cos(\omega_i t + \theta_i)$ with $i = 1$ or 2, can be substituted into Eqs. (6) and (7) to obtain the integral forms of the equations of motions for the following two eigenmodes:

$$\left(k_i - m\omega_i^2\right)\frac{A_i}{2} = \frac{1}{T}\int_0^T F(z)\cos(\omega_i t + \theta_i)dt, \tag{8}$$

$$\frac{b_i\omega_i A_i}{2} = \frac{1}{T}\int_0^T F(z)\sin(\omega_i t + \theta_i)dt. \tag{9}$$

When all the relevant forces represented in Eqs. (4)–(5b), including $F_{ts}(z)$, are substituted into the integrands presented in Eqs. (8) and (9) for the fundamental eigenmode ($i = 1$), the homodyne PiFM amplitude (A_m) measured at $\omega_m = \omega_1$ and

the heterodyne PiFM amplitude (A_s) at $\omega_s = \omega_m \pm \omega_2 = \omega_1$ can be derived as follows (see Appendix C for detailed calculations):

$$A_m = \frac{|F_m|}{\sqrt{m^2\left(\omega_1'^2 - \omega_m^2\right)^2 + (b_1'\omega_m)^2}}, \tag{10a}$$

$$A_s = \frac{|F_s|}{\sqrt{m^2\left(\omega_1'^2 - \omega_s^2\right)^2 + (b_1'\omega_s)^2}}, \tag{10b}$$

where $\omega_1' = \sqrt{(k_1 + k_c)/m}$ with $k_c \equiv -\frac{\partial F_c}{\partial z}|_{z_0}$ account for the frequency shift induced by the force gradient and $b_1' = b_1 + \Gamma$ is the effective damping coefficient of the fundamental eigenmode. A_m and A_s are proportional to the homodyne and heterodyne forces, respectively, and inversely proportional to the conservative force gradient and effective damping coefficient. This is the reason why the PiFM amplitudes, not forces, reach their maximum and then return to zero when the tip approaches the sample, as shown in Figs. 6(a) and 6(f), rather than when the *complex distance* is used, as insisted upon in a previous study [19]. This aspect will be fully addressed in the experimental results presented in Sec. III C.

D. Reconstruction of photoinduced thermal force from observation: Inverse problem

The amplitude and phase of the cantilever motion are experimentally accessible quantities. These quantities can be used to extract any conservative and nonconservative contributions to the cantilever. This approach is useful when there are several types of distance-dependent forces, particularly nonconservative forces, which are difficult to describe using a single explicit form of functions. The experimental observables can be related to the force gradient and damping coefficient present by evaluating the integrands in Eqs. (8) and (9) with the conservative and nonconservative forces:

$$k_c(z_0) \simeq -\frac{F_2}{A_2(z_0)}\sin\theta_2(z_0) - k_2 + m\omega_2^2, \tag{11}$$

$$\Gamma(z_0) \simeq \frac{F_2}{\omega_2 A_2(z_0)}\cos\theta_2(z_0) - b_2, \tag{12}$$

where $F_2 = k_2 A_{02}/Q_2$, $b_2 = k_2/(Q_2\omega_2)$, and A_{02} is the free oscillation amplitude at the second eigenmode. The quantities in Eqs. (11) and (12) can be obtained by measuring the second eigenmode amplitude (A_2) and the phase angle (θ_2). The analytically derived PiTFs can also be reconstructed by measuring the experimental observables. The following equation was obtained by implementing Eqs. (10a) and (10b) at the free space resonances (i.e., $\omega_1^2 = k_1/m$ and $\omega_2^2 = k_2/m$) after rewriting the forces in Eqs. (11) and (12) into a single form with relevant experimental parameters such as A_2, θ_2, k_j, and Q_j,

$$|F_j|^2 \approx \left(\frac{A_j k_2}{Q_2}\right)^2\left(\left(\frac{A_{02}}{A_2}\sin\theta_2\right)^2 + (\frac{\omega_j}{\omega_2})^2\left(\frac{\omega_j}{\omega_2}\frac{Q_2}{Q_j} + \frac{A_{02}}{A_2}\cos\theta_2 - 1\right)^2\right), \tag{13}$$

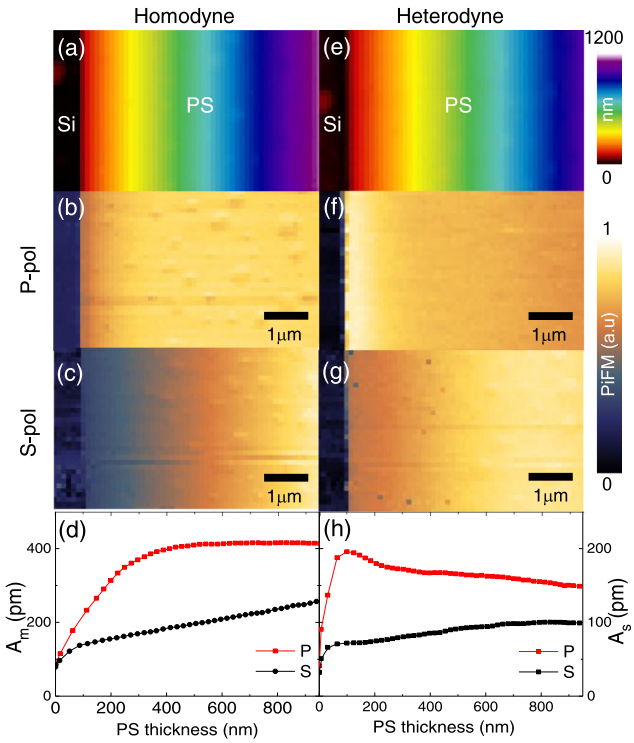

FIG. 4. Dependence of the PS thickness on the polarizations and PiFM measurement modes. A_m in the P (b) and S (c) polarizations and its topography (a). (d) Comparison of the line cuts of A_m in the P (red) and S (black) polarizations as a function of the PS thickness. A_s in the P (f) and S (g) polarizations and its topography (e). (h) Comparison of the line cuts of As in the P (red) and S (black) polarizations as a function of the PS thickness. The IR power at the 1492 cm^{-1} PS absorption resonance is 0.5 mW for the P polarization and 4 mW for the S polarization. The mechanical driving amplitude is ~2 nm at the second eigenmode (1.8 MHz) and PiFM detection is demodulated at the first eigenmode (300 kHz).

where $j = m, s$, ω_m(or ω_s) $= \omega_1$, and Q_m(or Q_s) $= Q_1$. The physical meaning of Eq. (13) is that the manifested photoinduced forces in Eqs. (5a) or (5b), which are expended on the resonant oscillation at the PiFM detection eigenmode and the interatomic tip-sample interaction, can be reconstructed by using the experimental observables.

III. RESULTS

A. Polarization dependence

The interesting feature of the tip-enhanced thermal expansion is the surface sensitive response, showing the peak behavior with respect to the sample thickness, compared to the bulk thermal expansion, which shows the gradual increase. The surface-sensitive measurement can be demonstrated with respect to the polarization of the beam because the near field is strongly enhanced at the tip end in the P polarization, while the field enhancement is reduced in the S polarization.

As shown in Fig. 4, the A_m and A_s of the PS wedge, which exhibits a thickness of 0–1000 nm, were obtained with respect to the P and S polarizations using PPP-NCHAu, an Au-coated noncontact cantilever (Nanosensors Inc.; $\omega_1 = 300$ kHz and

$k_1 = 30$ N/m). The IR power at the 1492 cm^{-1} PS absorption resonance for the S polarization (4 mW) was stronger than that for the P polarization (0.5 mW). The mechanical driving amplitude was ∼2 nm at the second eigenmode (1.8 MHz) and the PiFM detection was demodulated at the fundamental eigenmode (300 kHz). This case is hereinafter referred to as F2S1 for heterodyne PiFM, also known as a *sideband mode* (feedback at ω_2 and sideband mode at ω_1) and F2D1 for homodyne PiFM, also known as *direct mode* (feedback at ω_2 and direct mode at ω_1). This notation is quite useful for intuitively understanding the system configuration because there can be numerous combinations between the eigenmodes and the PiFM detection modes of the cantilever.

The A_m in the P polarization [Fig. 4(b)] shows the contribution of ΔL_{tot} when compared to that in the S polarization, which follows ΔL_b presented in Fig. 4(c). The difference becomes apparent when their line cuts are compared with respect to the thickness presented in Fig. 4(d). Although the A_m values in both polarizations increase with respect to the PS thickness, the slope at 200 nm in the P polarization (red) is considerably higher than that at the other sample thicknesses when compared to the S polarization measurement (black). The thickness behavior in the P polarization is very similar to the expected ΔL_{tot} (blue dashed line) in Fig. 2(a), while that in the S polarization corresponds well to the expected ΔL_b (red solid line) in Fig. 2(a). This result is well explained by Eq. (5a). The homodyne PiFM force dominantly follows ΔL_{tot}, which means that ΔL_t manifests in the P polarization on top of the thickness behavior of ΔL_b, while it is suppressed in the S polarization.

Figure 4(f) shows that the A_s in the P polarization is stronger at a small PS thickness but decreases as the thickness increases. However, the A_s in the S polarization gradually increases with respect to the PS thickness, as shown in Fig. 4(g). The difference is more noticeable when their line cuts are directly compared with respect to the thickness. Figure 4(h) shows the characteristic peak behavior of the P polarization (red), while that of the S polarization (black) gradually increases. This result is well explained by Eq. (5b). The tip-enhanced thermal expansion behavior (first and third terms) is dominant in the P polarization because of the strong tip-enhanced field, while it is suppressed in the S polarization, making the bulk thermal expansion (second term) dominant.

B. Small oscillation limit: Driving amplitude dependence

The oscillation amplitude can contribute to surface sensitivity. The tip-sample force can expand as $F_{\text{ts}}(z) \approx F_{\text{ts}}(z_0) + \frac{\partial F_{\text{ts}}}{\partial z}|_{z_0}(z - z_0) + \frac{1}{2}\frac{\partial^2 F_{\text{ts}}}{\partial z^2}|_{z_0}(z - z_0)^2 + O(z^3)$. In the small oscillation limit, the first derivative term of the tip-sample force is typically dominant over the second derivative term. However, as the oscillation of the carrier (mechanical) motion increases, the nonlinearity of the force increases and the second derivative term can be dominant. This indicates that the volume-sensitive nature (total thermal expansion) may still be outstanding in the heterodyne PiFM measurement by increasing the driving amplitude in accordance with Eq. (5b).

To observe the transition from the surface to volume, we measured the PS wedge in the P polarization by increasing the mechanical driving amplitude. Figure 5 clearly shows that

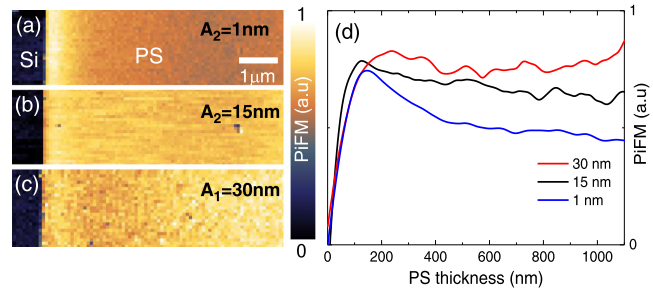

FIG. 5. Mechanical driving amplitude dependence with (a) $A_2 = 1$ nm, (b) $A_2 = 15$ nm in F2S1, and (c) $A_1 = 30$ nm in F1S2 for the P polarization as the PS thickness increases. (d) Normalized line cuts of the thickness dependence to displaying the transition from the surface-sensitive phase to the volume-sensitive phase.

the characteristic peak behavior (surface sensitive) included the gradually increased behavior (volume sensitive) as the driving amplitude increased from 1 nm [Fig. 5(a)] to 30 nm [Fig. 5(c)]. F2S1 obtained mechanical driving amplitudes of 1 and 15 nm, whereas F1S2 obtained a driving amplitude of 30 nm. The second eigenmode in our system could not obtain a driving amplitude of more than a few tens of nanometers because of the high motional stiffness of the second eigenmode (1180 N/m). However, the first eigenmode, which exhibited a stiffness of ∼30 N/m, could obtain such a driving amplitude. In both cases, the light modulation frequency was fixed at 2.1 MHz, the IR power was kept constant, and the mechanical driving and PiFM detection eigenmodes were simply switched. Figure 5(d) depicts a plot of the line cuts of the PS wedge, showing the transition from ΔL_t (surface sensitive) to ΔL_{tot} (volume sensitive). These results demonstrate that the surface sensitivity of PiFM requires a small oscillation amplitude under a few nanometers.

Notably, the probe sensitivity of the ith eigenmode, which corresponds to the minimum detectable force [31], is expressed as $F_{\text{min}_i} = \sqrt{4K_B T B k_i Q_i/\omega_i}$, where ω_i, Q_i, and k_i denote the resonance frequency, quality factor, and stiffness of the cantilever, respectively; B represents the system bandwidth; K_B denotes the Boltzmann constant; and T represents the absolute temperature. The sensitivity of the fundamental eigenmode is typically better than that of the second eigenmode, where $\omega_2 \approx 6.27\omega_1$, $k_2 \approx 40\,k_1$ and $Q_2 \approx 1.2 - 1.5\,Q_1$. When $B = 10$ Hz, the fundamental and second eigenmodes of PPP-NCHAu exhibit F_{min} of 0.08 and 0.18 pN, respectively, with $Q_1 = 370$ and $Q_2 = 483$. As shown in Figs. 5(a) and 5(c), F2S1 exhibits a better signal-to-noise ratio than F1S2.

C. Force-distance curve

The force reconstruction method is highly useful for understanding the nature of the force when several types of distance-dependent forces exist. The reconstructed force formula presented by Eq. (13), which is based on the experimental observables, considers all the forces acting on the cantilever as conservative and nonconservative forces with respect to the tip-sample distance. Therefore, any photoinduced forces can be quantitatively examined by measuring the

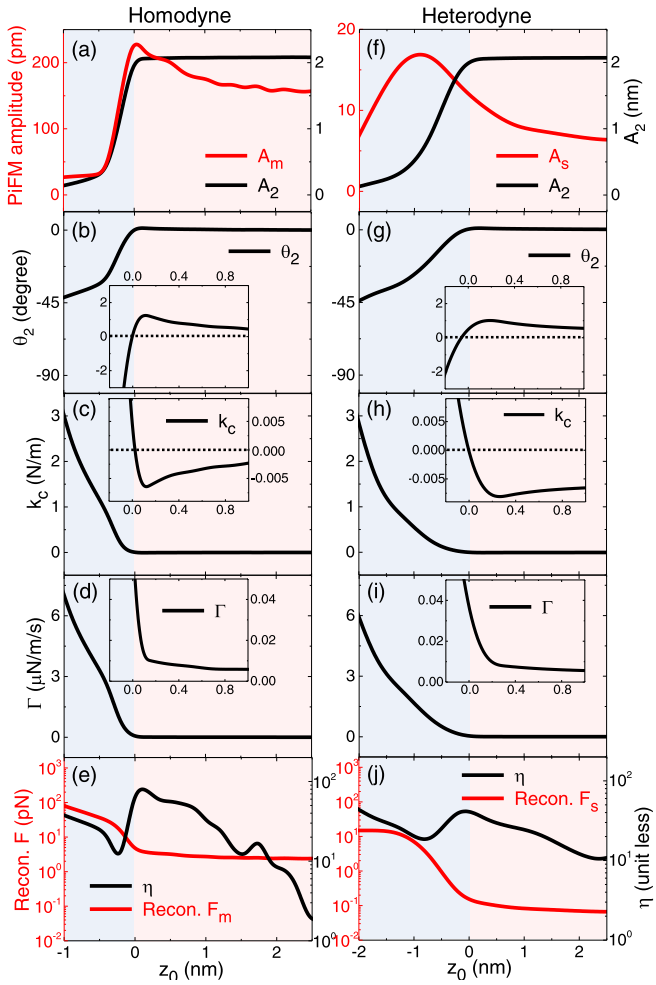

FIG. 6. Force-distance curves for the 133 nm PS film in the P polarization with respect to the PiFM measurement modes. (a) A_m (red) and A_2 (black), (b) θ_2, (c) k_c, (d) Γ, (e) η (black), and the reconstructed $|F_m|$ (red) for the PiFM homodyne measurement. (f) A_s (red) and A_2 (black), (g) θ_2, (h) k_c, (i) Γ, (j) η (black), and the reconstructed $|F_s|$ (red) for the PiFM heterodyne measurement. Each inset is the zoomed area near $z_0 \approx 0$. The red-shaded region is the noncontact (attractive) region, while the blue-shaded region is the contact (repulsive) region. The approach/retract speed is 12.5 nm/s.

force-distance curves. Because the force modulation cantilever is highly sensitive to the force-distance behavior with respect to the tip-sample distance, we used PPP-FMAu (Nanosensors Inc.), with $k_1 = 2.8$ N/m and $\omega_1 = 75$ kHz.

The force-distance curves for the PiFM homodyne and heterodyne measurements of the 133 nm PS film are plotted in Figs. 6(a)–6(e) and in Figs. 6(f)–6(j), respectively. The curve behaviors of A_2, θ_2, k_c, and Γ are similar to both the homodyne and heterodyne measurements because they have suffered from similar conservative and nonconservative forces. k_c decreases when the tip goes to zero ($z_0 \approx 0$) with a negative sign (attractive force gradient), as shown in the insets of Fig. 6(c) and Fig. 6(h), respectively. After surface tapping, k_c rapidly increases with a positive sign, reflecting the strong repulsive force gradient. This result is quite consistent with the theoretical expectation of $\Delta F_{\rm ts}$ in Fig. 3. However, since the magnitude of Γ depends on the approach/retract speed and the driving frequency of the cantilever, there is a minor increase in Γ in the noncontact region, as shown in the insets of Fig. 6(d) and Fig. 6(i), respectively. Note that this effect does not relate to the photoinduced interaction, because it is the same behavior even without light illumination. This demonstrates that the optomechanical damping effect that occurred in the noncontact region is negligible in the PiFM signal, which is contrary to the claim in a previous study [19].

The reconstructed $|F_m|$ and $|F_s|$ by Eq. (13) are plotted as a red solid line with a logarithmic scale in Figs. 6(e) and Fig. 6(j), respectively. Far from the surface, the relatively constant force around 3 pN in $|F_m|$ can be found to $z_0 \approx 1$ nm, which is mainly due to the constant scattering/photoacoustic forces [32,33]. However, the $|F_s|$ corresponds to the noise level (sub 0.1 pN) in that range. This is because heterodyne PiFM measures the force gradient of the light-modulated force, which can remove the constant photoacoustic/scattering forces. When the tip approaches the surface, $|F_m|$ and $|F_s|$ gradually increase near $z_0 \approx 0$ nm, which corresponds to the PiTF mediated by the attractive van der Waals force gradient [15]. A_m reaches its maximum while A_s does near $z_0 \approx -1$ nm in the repulsive tapping region (blue-shaded area). Since A_s is also proportional to A_2 as in Eq. (5b), it can reach its maximum further inside the attractive (repulsive) region by employing a soft (stiff) cantilever which is less (more) resistant to the jump-to-contact effect.

The ratio of the conservative to nonconservative force contribution in the reconstructed $|F_m|$ and $|F_s|$, which can be expressed as $\eta \equiv k_c^2/(\Gamma\omega_1)^2$, are plotted as a black solid line with a logarithmic scale in Figs. 6(e) and 6(j), respectively. Both cases, the conservative force contribution is typically one order of magnitude higher than the nonconservative force contribution, showing that η is greater than unity in both the attractive and repulsive regions. This demonstrates that the conservative interaction is dominant over the nonconservative interaction in the measured PiFM signal.

IV. DISCUSSION

The thermal expansion at the tip-sample junction can be described as surface-sensitive (near-field) and volume-sensitive (far-field) thermal expansions. The change in the tip-sample distance due to the thermal expansions in dynamic PiFM generates homodyne and heterodyne PiFM forces that can distinguish between surface-sensitive and volume-sensitive thermal responses. The tip-enhanced thermal expansion (surface sensitive) can be probed via the heterodyne PiFM measurement under the P polarization. The bulk thermal expansion (volume sensitive) can be probed via the PiFM homodyne measurement under the S polarization. Moreover, we observed that the surface-sensitive response in the PiFM heterodyne measurement included a volume-sensitive response when the driving amplitude was increased. This explains that a small oscillation amplitude (under a few nanometers) is a critical parameter affecting the high surface sensitivity of PiFM.

Moreover, the magnitude of the tapping force can contribute to surface sensitivity. When the tip strongly taps the sample, the strong repulsive force acts as an impulse force

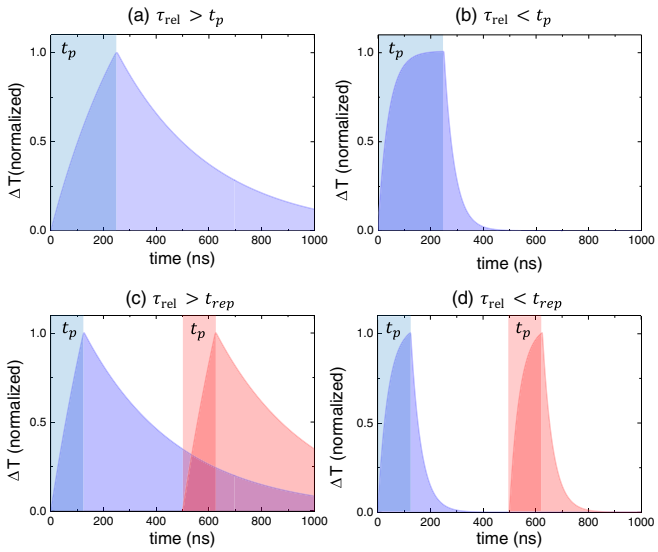

FIG. 7. Time-dependent temperature rise when (a) $\tau_{rel} > t_p$ and (b) $\tau_{rel} < t_p$. Time-dependent temperatures in the repeatable pulses when (c) $\tau_{rel} > t_{rep}$ and (d) $\tau_{rel} < t_{rep}$. The rectangular shaded area is the pulse width.

which increases the nonlinearity of the interatomic tip-sample force. Thus, a strong tapping force can also increase the volume response [second derivative term in Eq. (5b)] during the heterodyne PiFM measurement. Noncontact/gentle tapping can be another critical condition affecting surface sensitivity. Note that the tapping-mode PTIR technique, which has been recently introduced for surface-sensitive thermal measurements in PTIR, is very similar to the PiFM technique, but it mainly functions in the hard-tapping region [18]. However, our analysis results points out that the hard tapping may include the bulk response in the tapping-mode PTIR measurements.

The surface sensitivity of the thermal response can also be controlled by changing the repetition period (t_{rep}) of a laser beam. The temperature change caused by a laser pulse should be allowed to cool to zero before illuminating the next laser pulse. However, when τ_{rel} is longer than t_{rep}, the temperature change still remains so thermal modulation depth decreases, as shown in Fig. 7(c). The calculation details lie in the Appendix A. Because the heating volume of the bulk thermal expansion is proportional to the total sample volume, τ_{rel} of ΔT_b for the thick sample becomes longer than t_{rep} during the high-frequency modulation. Conversely, because the heating volume of the tip-enhanced thermal expansion is limited by the thermal diffusion length of Δl_p, the τ_{rel} of ΔT_t may still be comparable to t_{rep}. This effect makes that the thermal modulation depth of ΔT_b is smaller than that of ΔT_t. Thus, high-frequency light modulation may be another condition that affects surface sensitivity.

The high-frequency light modulation effect can occur in the PiFM measurement modes. The S polarization measurement via the heterodyne PiFM ($\omega_m = 2\pi \times 2.1$MHz) presented in Fig. 4(h) (black) exhibits a lower slope with respect to the thickness than that via the homodyne PiFM ($\omega_m = 2\pi \times 300$kHz) shown in Fig. 4(d) (black). If the force gradients and the damping coefficients at a certain tip-sample distance can be regarded as constant variables because both PiFM measurement modes only observe ΔL_b in the S polarization measurement as a variable parameter in Eqs. (5a) and (5b), the reduced response in the high-frequency light modulation may support this hypothesis. In addition, a recent study [18] claims that the surface sensitivity of PTIR is caused by the high-frequency light modulation of the thermal expansions. This result also suggests that the high-frequency thermal modulation could be the additional reason why heterodyne PiFM is much more surface sensitive than homodyne PiFM.

Lastly, the way to control the thermal responses may allow us to separate the PiDF from the PiTF or vice versa. Since the PiDF is proportional to the polarizability while the PiTF follows the absorption coefficient, some samples such as phonon polaritonic materials may have spectrally different force curve behaviors. For example, the quartz has the far-field absorption resonance near 1070 cm^{-1} [34] while it has the near-field resonance under the metallic tip-sample geometry near 1130 cm^{-1} [35]. Since the quartz typically has a very small thermal expansion coefficient (0.55×10^{-6}/K), the PiTF of ΔL_t may be ignorable in the measured IR spectral range. In this case, the PiDF, which follows the near-field resonance spectrum, may be spectrally deviated from the PiTF of ΔL_b, which follows the far-field absorption spectrum, by controlling the parameters such as the driving amplitude, tapping force, and light modulation frequency.

V. CONCLUSION

Herein, we present comprehensive theoretical explanations and experimental demonstrations of the PiTFs at the tip-sample junction for the surface and volume-sensitive responses when the PiDF is small enough. The near-field tip-enhanced thermal expansion (surface) and the far-field bulk thermal expansion (volume) can be distinguished using the heterodyne and homodyne PiFM measurements, respectively. Moreover, we discovered that the key factors for the surface sensitivity originated from the field enhancement at the tip end, the small oscillation of the driving amplitude, and the magnitude of tapping force. We also discussed some additional parameters such as the pulse width and the light modulation frequency. According to our study, any damping effect including optomechanical damping is ignorable to the PiFM surface sensitivity in the mid-IR. The experimental results for the polarization, driving amplitude, and force-distance curve successfully support the theoretically expected PiTFs. The analysis method used in this paper can be applied to other spectroscopic nanoimaging tools, such as resonance-enhanced/tapping-mode PTIR and peak force infrared microscopy [36]. We believe that our paper can help understand the nature of the photoinduced forces in optomechanical spectroscopic nanoimaging studies.

ACKNOWLEDGMENTS

This study was supported by the National Research Foundation of Korea (NRF) grant funded by the Korea government (MSIT; Grant No. 2022R1C1C1008766) and the

Nano Material Technology Development Program (Grant No. 2016M3A7B6908929).

APPENDIX A: TIME DEPENDENT TEMPERATURE OF A HEATED THIN FILM

In general, the temperature rise inside the sample with a heating source Q_0 is described by the heat diffusion equation

$$\rho C\frac{dT}{dt'}-\kappa_{\rm eff}\nabla^2 T=\frac{Q_0}{V}, \tag{A1}$$

where ρ, C and $\kappa_{\rm eff}$ are the density, the heat capacity, and the effective thermal conductivity. The source Q_0 is linked to the absorbed power from laser irradiation in the sample, given as $Q_0=\int_0^{t_p}P_{\rm abs}(t')dt'$. V is the heating volume.

Considering the absorption during t_p, the one-dimensional heat diffusion equation of Eq. (A1) may be solved by using the separation of variables of the temperature with the product of the time and position, which can be given as

$$T^-(z',t')=T_t^-(t')T_z^-(z')\ \ (0<t'<t_p), \tag{A2}$$

$$T^+(z',t')=T_t^+(t')T_z^+(z')\ \ (t_p<t'). \tag{A3}$$

Substituting the above equations into the heat diffusion equation, the temperature after heating time ($t_p<t'$) is recast as

$$\frac{1}{T_t^+(t')}\frac{dT_t^+(t')}{dt'}-\frac{\kappa_{\rm eff}}{\rho C}\frac{1}{T_z^+(z')}\frac{d^2T_z^+(z')}{dz'^2}=0. \tag{A4}$$

Let's set the z'-dependent variables as τ^+. The time-dependent temperature is derived as

$$\frac{\kappa_{\rm eff}}{\rho C}\frac{1}{T_z^+(z')}\frac{d^2T_z^+(z')}{dz'^2}\equiv-\frac{1}{\tau^+}, \tag{A5}$$

$$\frac{dT_t^+(t')}{dt'}=-\frac{1}{\tau^+}T_t^+(t'), \tag{A6}$$

$$T_t^+(t')=T_1e^{-t'/\tau^+}. \tag{A7}$$

By setting the t'-dependent variables as ζ_+, the thermal mode of the position dependent temperature is derived as

$$\frac{1}{T_z^+(z')}\frac{d^2T_z^+(z')}{dz'^2}\equiv-\zeta_+^2, \tag{A8}$$

$$T_z^+(z')=T_2\cos(\zeta_+(z'-z_0')). \tag{A9}$$

Considering the low-heat capacity and thermal conductivity of the air, one can define the boundary condition of no heat source and no heat flow to the air as below:

$$j=-\kappa_{\rm eff}\frac{dT}{dz'}|_{z'=l_z}=0. \tag{A10}$$

The substrate is assumed to be at constant temperature, which without loss of generality, is chosen to be $T(-0,t')=0$. In the presence of an interfacial thermal resistance S between the sample and the constant temperature substrate boundary (located at $z'=0$), the heat flux is continuous:

$$j=-\kappa_{\rm eff}\frac{dT}{dz'}|_{z'=0}=-S[T(+0,t')-T(-0,t')]. \tag{A11}$$

By considering the above two boundary conditions under the separation of variables method, the thermal mode of the time-dependent temperature is calculated as

$$T^+(z',t')=T_0e^{-t'/\tau^+}\cos(\zeta_+(z'-l_z)). \tag{A12}$$

$$\kappa_{\rm eff}\zeta_+\sin(\zeta_+l_z)=S\cos(\zeta_+l_z), \tag{A13}$$

with the variables of

$$\tau^+=\frac{\rho C}{\kappa_{\rm eff}}\frac{1}{\zeta_+^2}, \tag{A14}$$

$$\zeta_+=\frac{S}{\kappa_{\rm eff}}\cot(\zeta_+l_z). \tag{A15}$$

For large S, $\zeta_+\approx\pi/2l_z$.

In the same manner, when the sample is heated up during t_p, the time-dependent temperature ($0<t'<t_p$) is derived as below:

$$\frac{dT_t^-(t')}{dt'}-\frac{\kappa_{\rm eff}}{\rho C}\frac{1}{T_z^-(z')}\frac{d^2T_z^-(z')}{dz'^2}=\frac{Q_0}{T_z^-(z')\rho CV}.$$

Then the temperature can be recast as

$$T_t^-(t')=P_0\tau^-+ge^{-t'/\tau^-}, \tag{A16}$$

with the variables of

$$\frac{1}{\tau^-}\equiv-\frac{\kappa_{\rm eff}}{\rho C}\frac{1}{T_z^-(z')}\frac{d^2T_z^-(z')}{dz'^2}, \tag{A17}$$

$$P_0\equiv\frac{Q_0}{\rho CV}. \tag{A18}$$

For the initial condition of $T(z',0)=0$,

$$T_t^-(t')=P_0\tau^-[1-e^{-t'/\tau^-}]. \tag{A19}$$

The position-dependent differential equation is recast as

$$\zeta_-^2\equiv-\frac{1}{T_z^-(z')}\frac{d^2T_z^-(z')}{dz'^2}, \tag{A20}$$

where $\zeta_-^2=\rho C/\kappa_{\rm eff}\tau^-$. Then, the solution of the above equation can be derived as

$$T_z^-(z')=T_3\cos(\zeta_-(z'-l_z)). \tag{A21}$$

According to the boundary condition of $T^-(z',t_p)=T^+(z',t_p)$,

$$P_0\tau^-[1-e^{-t_p/\tau^-}]T_z^-(z')=Ae^{-t_p/\tau^+}T_z^+(z'),$$

$$A=P_0\tau^-[1-e^{-t_p/\tau^-}]e^{t_p/\tau^+}T_z^-(z')/T_z^+(z'),$$

$$T^+(z',t')=\frac{Q_0\tau^-}{\rho CV}[1-e^{-t_p/\tau^-}]e^{-(t-t_p)/\tau^+}T_z^-(z').$$

If we assume $\tau_+\simeq\tau_-\equiv\tau_{\rm rel}$, the complete time-dependent temperature change is given as

$$\Delta T(z',t')=\begin{cases}\Delta T_{\max}e^{-(t'-\tau_p)/\tau_{\rm rel}}\cos(\zeta(z'-l_z))(t'>\tau_p)\\ \Delta T_{\max}\frac{1-e^{-t'/\tau_{\rm rel}}}{1-e^{-t_p/\tau_{\rm rel}}}\cos(\zeta(z'-l_z))\ \ (t'<\tau_p),\end{cases}$$

with the variables of

$$\Delta T_{\max} = \frac{Q_0 \tau_{\rm th}}{\rho C V}, \tag{A22}$$

$$\tau_{\rm th} = \tau_{\rm rel}(1 - e^{-t_p/\tau_{\rm rel}}), \tag{A23}$$

$$\tau_{\rm rel} = \frac{4}{\pi^2}\frac{\rho C}{\kappa_{\rm eff}} l_z^2, \tag{A24}$$

where t_p, $\tau_{\rm rel}$, and ζ are the laser pulse width, relaxation (cooling) time, and thermal mode shape. The $\tau_{\rm th}$ can be understood as the effective thermalization time considering both the heating and cooling time. Since the temperature is directly proportional to the $\tau_{\rm th}$, the temperature typically shows saturated behavior as the function of the sample thickness, which is shown in Fig. 2 as black solid lines.

Equations (A22) to (A24) imply that both the heating and cooling time simultaneously contribute to the temperature of the sample. There are three important times regarding the maximum temperature: one is the heating time, which corresponds to the pulse width, another is the relaxation (cooling) time, which is the time for the sample to reach the equilibrium with the environment as determined by the thermal diffusion process. If the relaxation time is longer than the pulse width (thick sample), the temperature is relatively proportional to the pulse width as in Fig. 7(a). However, if the $\tau_{\rm rel}$ is much shorter than the t_p (thin sample) or the t_p is much longer than the $\tau_{\rm rel}$ (long pulse width), the temperature is saturated as in Fig. 7(b). This behavior can be understood as the effective relaxation time $\bar{\tau}_{\rm rel}$ in Eq. (A23), which means the time to get the equilibrium by considering both the heating and cooling process.

The final important time is the repetition period for the pulsed laser. When the relaxation time is longer than the repetition period $\tau_{\rm rel} > t_{\rm rel}$, the sample is not fully cooled down, so the temperature change gets saturated like as the process of Fig. 7(c). This means that the high repetition rate reduces the depth of the thermal modulation. To avoid this issue, the relaxation time should be smaller than the repetition period as in Fig. 7(d).

APPENDIX B: FREQUENCY-DEPENDENT THERMAL EXPANSIONS AND PHOTOINDUCED THERMAL FORCES IN DYNAMIC TIP MOTIONS

The heating source, Q_0, depends on the geometry at the tip-sample junction. The light-absorbed power at the tip-sample gap distance, z, can be expressed as below by considering the optical field as the far-field E_f and near-field E_n,

$$Q_0 = \int P_{\rm abs}(z) dt', \tag{B1}$$

$$P_{\rm abs}(z) = \int a_{\rm abs} \frac{1}{2} c\varepsilon_0 |E(z')|^2 dV_{\rm abs}, \tag{B2}$$

$$E(z') = E_f + E_n(z'), \tag{B3}$$

where $a_{\rm abs}$, z', λ, c, and E are the absorption coefficient, the coordinate along the sample thickness, the wavelength, the speed of light, and the electric field inside the sample, respectively. The absorption coefficient is given as $a_{\rm abs} = \frac{4\pi}{\lambda}{\rm Im}\{\bar{n}\}$, where $\bar{n}$ is the complex refractive index. The far field inside the sample is calculated by $E_f = (1-R)E_0$, where R and E_0 are the Fresnel's reflection coefficient and the incident far field. In this paper, we consider a weakly absorptive molecular vibration that is $(1-R)^2 \approx \frac{9{\rm Re}\{\bar{n}\}}{({\rm Re}\{\bar{n}\}^2+2)^2}$ [37]. The near field inside the sample is calculated under the air/sample/substrate geometry by using the finite dipole method reported in previous studies [26,27].

If we assume that the thermal expansion is proportional to the temperature change, the calculation of the thermal expansion can be simplified by regarding the temperature change of $\Delta T_{\max}$. In this case, the maximum thermal expansion is given as below:

$$\Delta L_{\rm tot}(z) = \sigma l_z \Delta T_{\max} \tag{B4}$$

$$\approx \frac{\sigma l_z \tau_{\rm th}}{\rho C V_{\rm heat}} \int a_{\rm abs} \frac{1}{2} c\varepsilon_0 (|E_f|^2 + |E_n(z')|^2) dV_{\rm abs}$$

$$\equiv \Delta L_b + \Delta L_t(z), \tag{B5}$$

with $\tau_{\rm th} = \tau_{\rm rel}(1 - e^{-t_p/\tau_{\rm rel}})$. σ, l_z and $\tau_{\rm th}$ are the linear thermal expansion coefficient, the heating length of the sample and the effective relaxation time. When the laser beam repeatedly illuminates the tip-sample junction at frequency ω_m as $I(t) = |E|^2 \sin(\omega_m t)$, the time-dependent thermal expansion with an harmonic assumption can be given as

$$\Delta L_{\rm tot}(t) = \Delta L_{\rm tot}(z) \sin(\omega_m t + \theta_m)$$

$$= (\Delta L_b + \Delta L_t(z)) \sin(\omega_m t + \theta_m). \tag{B6}$$

If we consider two eigenmodes of the cantilever system, when the tip is dynamically driven at a frequency (ω_2), the coordinates of the first two eigenmodes, the homodyne motion at ω_m and heterodyne motion at $\omega_s = \omega_m \pm \omega_2$ are $z_1(t)$, $z_2(t)$, $z_m(t)$, and $z_s(t)$. Then the instantaneous tip position can be expressed as $z(t) \approx z_0 + z_1(t) + z_2(t) + z_m(t) + z_s(t) - \Delta L_{\rm tot}(t)$, where z_0 is the average tip-sample distance. The distance dependent tip-enhanced thermal expansion can be expanded by the Taylor series as $\Delta L_t(z) \approx \Delta L_t(z_0) + \frac{\partial \Delta L_t}{\partial z}(z - z_0) + O(z^2)$ in the small oscillation limit. By assuming the harmonic motions of $z_1(t) = A_1 \cos(\omega_1 + \theta_1)$, $z_2(t) = A_2 \cos(\omega_2 + \theta_2)$, $z_m(t) = A_m \cos(\omega_m + \theta_m)$, and $z_s(t) = A_s \cos(\omega_s + \theta_s)$, the time-dependent thermal expansion can be rewritten as

$$\Delta L_b(t) = \Delta L_b \sin(\omega_m t + \theta_m), \tag{B7}$$

$$\Delta L_t(t) = \Delta L_t(z) \sin(\omega_m t + \theta_m)$$

$$\approx \Delta L_t(z_0) \sin(\omega_m t + \theta_m)$$

$$+ \frac{1}{2} \frac{\partial \Delta L_t}{\partial z}|_{z_0} A_2 \sin(\omega_s t + \theta_s), \tag{B8}$$

where $\omega_s = \omega_m \pm \omega_2$ and $\theta_s = \theta_m \pm \theta_2$.

Because the thermal expansion changes the tip-sample distance, the tip-sample interaction force can mediate the response to the tip. The force can be expanded in the small oscillation limit as below:

$$F_{ts}(z) \approx F_c(z_0) + \Gamma(z_0)\dot{z} + \frac{\partial F_c}{\partial z}|_{z_0}(z - z_0)$$

$$+ \frac{1}{2} \frac{\partial^2 F_c}{\partial z^2}|_{z_0}(z - z_0)^2 + \ldots. \tag{B9}$$

By substituting $z - z_0 = z_1 + z_2 + z_m + z_s - \Delta L_{\rm tot}(t)$ into the expanded forces, the frequency-dependent tip-sample force can be recast as

$$\begin{aligned} F_{ts}(z) \approx F_c &+ \Gamma(\dot{z}_1 + \dot{z}_2 + \dot{z}_m + \dot{z}_s - \Delta\dot{L}_{\rm tot}) \\ &+ \frac{\partial F_c}{\partial z}(z_1 + z_2 + z_m + z_s - \Delta L_{\rm tot}) \\ &- \frac{\partial^2 F_c}{\partial z^2}|_{z_0} z_2 \Delta L_{\rm tot} + ... \end{aligned} \tag{B10}$$

Separating the frequency-dependent terms at each frequency at ω_m and ω_s by ignoring the higher order derivative terms, one can obtain the frequency-dependent PiTFs as below:

$$F_m \approx -\frac{\partial F_c}{\partial z}\Delta L_{\rm tot}\sin(\omega_m t + \theta_m) - \Gamma\omega_m \Delta L_{\rm tot}\cos(\omega_m t + \theta_m), \tag{B11}$$

$$\begin{aligned} F_s \approx &-\frac{1}{2}\left(\frac{\partial F_c}{\partial z}\frac{\partial \Delta L_t}{\partial z}|_{z_0} + \frac{\partial^2 F_c}{\partial z^2}\Delta L_{\rm tot}\right)A_2\sin(\omega_s t + \theta_s) \\ &- \frac{1}{2}\Gamma\omega_s\frac{\partial \Delta L_t}{\partial z}|_{z_0} A_2\cos(\omega_s t + \theta_s), \end{aligned} \tag{B12}$$

where F_m is the PiFM homodyne force at ω_m and F_s is the PiFM heterodyne force at $\omega_s = \omega_m \pm \omega_2$.

APPENDIX C: EVALUATING INTEGRAL EQUATIONS OF MOTIONS

Let's first solve the mechanical driving amplitude and phase for the second eigenmode ($i = 2$). The integrands in Eqs. (8) and (9) can be calculated with high accuracy over the period $T = 2\pi p_1/\omega_1 = 2\pi p_s/\omega_s = 2\pi p_m/\omega_m$, where p_1, p_s, and p_m are the commensurable integers; i.e., $\omega_1/\omega_s = p_1/p_s$, $\omega_1/\omega_m = p_1/p_m$, and $\omega_s/\omega_m = p_s/p_m$. The physical meaning of the commensurable integers is to increase the measuring time. Then, the ω_2-dependent force is only survived in the integrands by one period integration because of trigonometric relation, which are rewritten as

$$\left(k_2 - m\omega_2^2\right)\frac{A_2}{2} = \frac{1}{T}\int_0^T\left(\frac{\partial F_c}{\partial z}z_2 + F_2(t)\right)\cos(\omega_2 t + \theta_2)dt, \tag{C1}$$

$$\frac{b_2\omega_2 A_2}{2} = \frac{1}{T}\int_0^T(\Gamma\dot{z}_2 + F_2(t))\sin(\omega_2 t + \theta_2)dt, \tag{C2}$$

where $F_2(t) = F_2\sin\omega_2 t$. By calculating the integrands with one period, the equations are recast as

$$\left(k_2 - \frac{\partial F_c}{\partial z} - m\omega_2^2\right)A_2 = -F_2\sin\theta_2, \tag{C3}$$

$$(b_2 + \Gamma)\omega_2 A_2 = F_2\cos\theta_2. \tag{C4}$$

Then, the mechanically driving amplitude and phase are derived as

$$A_2(\omega_2) = \frac{F_2}{\sqrt{m^2\left(\omega_2'^2 - \omega_2^2\right)^2 + (b_2'\omega_2)^2}}, \tag{C5}$$

$$\theta_2(\omega_2) = -\tan^{-1}\left(\frac{m\left(\omega_2'^2 - \omega_2^2\right)}{b_2'\omega_2}\right), \tag{C6}$$

where $\omega_2' = \sqrt{(k_2 + k_c)/m}$ with $k_c \equiv -\frac{\partial F_c}{\partial z}|_{z_0}$ and $b_2' = b_2 + \Gamma$.

By substituting the expanded tip-sample forces in Eq. (B10) into Eqs. (8) and (9), we can calculate the integral forms of equations at the first eigenmodes ($i = 1$) for the PiFM homodyne and heterodyne measurements. Then the integrand can be recast as

$$\left(k_1 - m\omega_1^2\right)\frac{A_1}{2} = \frac{1}{T}\int_0^T\left(\frac{\partial F_c}{\partial z}z_1 + F_j\right)\cos(\omega_1 t + \theta_1)dt, \tag{C7}$$

$$\frac{b_1\omega_1 A_1}{2} = \frac{1}{T}\int_0^T(\Gamma\dot{z}_1 + F_j)\sin(\omega_1 t + \theta_1)dt, \tag{C8}$$

where $j = m, s$. For the homodyne measurement at $\omega_m = \omega_1$, the integrands are calculated as below:

$$\begin{aligned} \left(k_1 - \frac{\partial F_c}{\partial z} - m\omega_1^2\right)A_1 \approx &\frac{\partial F_c}{\partial z}\Delta L_{\rm tot}\sin(\theta_1 - \theta_m) \\ &- \Gamma\omega_m\Delta L_{\rm tot}\cos(\theta_1 - \theta_m), \end{aligned} \tag{C9}$$

$$\begin{aligned} (b_1 + \Gamma)\omega_1 A_1 \approx &-\frac{\partial F_c}{\partial z}\Delta L_{\rm tot}\cos(\theta_1 - \theta_m) \\ &- \Gamma\omega_m\Delta L_{\rm tot}\sin(\theta_1 - \theta_m). \end{aligned} \tag{C10}$$

By squaring and summing the Eqs. (C9) and (C10), the PiFM homodyne amplitude (A_m) and phase ($\bar{\theta}_m$) are derived as

$$A_m \equiv A_1(\omega_m) = \frac{|F_m|}{\sqrt{m^2\left(\omega_1'^2 - \omega_m^2\right)^2 + (b_1'\omega_m)^2}}, \tag{C11}$$

$$\bar{\theta}_m \equiv \theta_1(\omega_m) = \theta_m + \tan^{-1}\left(\frac{-aA + bB}{bA + aB}\right), \tag{C12}$$

where $\omega_1' = \sqrt{(k_1 + k_c)/m}$, $b_1' = b_1 + \Gamma$, $a = \frac{\partial F_c}{\partial z}\Delta L_{\rm tot}$, $b = \Gamma\omega_m\Delta L_{\rm tot}$, $A = k_1 + k_c - m\omega_1^2$, and $B = b_1'\omega_1$. With the same manner, the heterodyne amplitude (A_s) and phase ($\bar{\theta}_s$) at $\omega_s = \omega_m \pm \omega_2 = \omega_1$ are derived as

$$A_s \equiv A_1(\omega_s) = \frac{|F_s|}{\sqrt{m^2\left(\omega_1'^2 - \omega_s^2\right)^2 + (b_1'\omega_s)^2}}, \tag{C13}$$

$$\bar{\theta}_s \equiv \theta_1(\omega_s) = \theta_s + \tan^{-1}\left(\frac{-a'A + b'B}{b'A + a'B}\right), \tag{C14}$$

where $\theta_s = \theta_m \pm \theta_2$, $a' = \frac{A_2}{2}(\frac{\partial F_c}{\partial z}\frac{\partial \Delta L_t}{\partial z} + \frac{\partial^2 F_c}{\partial z^2}\Delta L_{\rm tot})$, $b' = \Gamma\omega_s\frac{1}{2}\frac{\partial \Delta L_t}{\partial z}A_2$, $A = k_1 + k_c - m\omega_1^2$, and $B = b_1'\omega_1$.

[1] C. Yang, J. Chen, X. Ji, T. P. Pollard, X. Lü, C.-J. Sun, S. Hou, Q. Liu, C. Liu, T. Qing *et al.*, Aqueous li-ion battery enabled by halogen conversion–intercalation chemistry in graphite, Nature (London) **569**, 245 (2019).

[2] E. Ventosa, P. Wilde, A.-H. Zinn, M. Trautmann, A. Ludwig, and W. Schuhmann, Understanding surface reactivity of Si electrodes in Li-ion batteries by *in operando* scanning electrochemical microscopy, Chem. Commun. **52**, 6825 (2016).

[3] X. Su, Q. Wu, J. Li, X. Xiao, A. Lott, W. Lu, B. W. Sheldon, and J. Wu, Silicon-based nanomaterials for lithium-ion batteries: A review, Adv. Energy Mater. **4**, 1300882 (2014).

[4] R. C. Massé, C. Liu, Y. Li, L. Mai, and G. Cao, Energy storage through intercalation reactions: Electrodes for rechargeable batteries, Natl. Sci. Rev. **4**, 26 (2017).

[5] M.-k. Jo, H. Heo, J.-H. Lee, S. Choi, A. Kim, H. B. Jeong, H. Y. Jeong, J. M. Yuk, D. Eom, J. Jahng *et al.*, Enhancement of photoresponse on narrow-bandgap Mott insulator $\alpha - RuCl_3$ via intercalation, ACS Nano **15**, 18113 (2021).

[6] A. A. Sifat, J. Jahng, and E. O. Potma, Photo-induced force microscopy (PiFM)–principles and implementations, Chem. Soc. Rev. **51**, 4208 (2022).

[7] J. Jahng, D. A. Fishman, S. Park, D. B. Nowak, W. A. Morrison, H. K. Wickramasinghe, and E. O. Potma, Linear and nonlinear optical spectroscopy at the nanoscale with photoinduced force microscopy, Acc. Chem. Res. **48**, 2671 (2015).

[8] I. Rajapaksa, K. Uenal, and H. K. Wickramasinghe, Image force microscopy of molecular resonance: A microscope principle, Appl. Phys. Lett. **97**, 073121 (2010).

[9] J. Jahng, J. Brocious, D. A. Fishman, F. Huang, X. Li, V. A. Tamma, H. K. Wickramasinghe, and E. O. Potma, Gradient and scattering forces in photoinduced force microscopy, Phys. Rev. B **90**, 155417 (2014).

[10] J. Jahng, F. T. Ladani, R. M. Khan, and E. O. Potma, Photo-induced force for spectroscopic imaging at the nanoscale, Proc. SPIE **9764**, 97641J (2016).

[11] J. Yamanishi, H. Yamane, Y. Naitoh, Y. J. Li, N. Yokoshi, T. Kameyama, S. Koyama, T. Torimoto, H. Ishihara, and Y. Sugawara, Optical force mapping at the single-nanometre scale, Nat. Commun. **12**, 3865 (2021).

[12] J. Jahng, F. T. Ladani, R. M. Khan, X. Li, E. S. Lee, and E. O. Potma, Visualizing surface plasmon polaritons by their gradient force, Opt. Lett. **40**, 5058 (2015).

[13] A. Ambrosio, M. Tamagnone, K. Chaudhary, L. A. Jauregui, P. Kim, W. L. Wilson, and F. Capasso, Selective excitation and imaging of ultraslow phonon polaritons in thin hexagonal boron nitride crystals, Light Sci. Appl. **7**, 27 (2018).

[14] M. Tamagnone, A. Ambrosio, K. Chaudhary, L. A. Jauregui, P. Kim, W. L. Wilson, and F. Capasso, Ultra-confined mid-infrared resonant phonon polaritons in van der Waals nanostructures, Sci. Adv. **4**, eaat7189 (2018).

[15] J. Jahng, E. O. Potma, and E. S. Lee, Tip-enhanced thermal expansion force for nanoscale chemical imaging and spectroscopy in photoinduced force microscopy, Anal. Chem. **90**, 11054 (2018).

[16] L. Wang, H. Wang, D. Vezenov, and X. G. Xu, Direct measurement of photoinduced force for nanoscale infrared spectroscopy and chemical-sensitive imaging, J. Phys. Chem. C **122**, 23808 (2018).

[17] J. J. Schwartz, D. S. Jakob, and A. Centrone, A guide to nanoscale IR spectroscopy: Resonance enhanced transduction in contact and tapping mode AFM-IR, Chem. Soc. Rev. **51**, 5248 (2022).

[18] J. Mathurin, A. Deniset-Besseau, D. Bazin, E. Dartois, M. Wagner, and A. Dazzi, Photothermal AFM-IR spectroscopy and imaging: Status, challenges, and trends, J. Appl. Phys. **131**, 010901 (2022).

[19] M. A. Almajhadi, S. M. A. Uddin, and H. K. Wickramasinghe, Observation of nanoscale opto-mechanical molecular damping as the origin of spectroscopic contrast in photo induced force microscopy, Nat. Commun. **11**, 5691 (2020).

[20] B. Kim and E. O. Potma, Laser heating of cantilevered tips: Implications for photoinduced force microscopy, Phys. Rev. B **100**, 195416 (2019).

[21] J. Jahng, E. O. Potma, and E. S. Lee, Nanoscale spectroscopic origins of photoinduced tip–sample force in the midinfrared, Proc. Natl. Acad. Sci. **116**, 26359 (2019).

[22] F. T. Ladani and E. O. Potma, Dyadic Green's function formalism for photoinduced forces in tip-sample nanojunctions, Phys. Rev. B **95**, 205440 (2017).

[23] H. U. Yang and M. B. Raschke, Resonant optical gradient force interaction for nano-imaging and -spectroscopy, New J. Phys. **18**, 053042 (2016).

[24] X. Zhang, J. Qiu, J. Zhao, X. Li, and L. Liu, Complex refractive indices measurements of polymers in infrared bands, J. Quant. Spectrosc. Radiat. Transfer **252**, 107063 (2020).

[25] J. Jahng, H. Yang, and E. S. Lee, Substructure imaging of heterogeneous nanomaterials with enhanced refractive index contrast by using a functionalized tip in photoinduced force microscopy, Light Sci. Appl. **7**, 73 (2018).

[26] A. Cvitkovic, N. Ocelic, and R. Hillenbrand, Analytical model for quantitative prediction of material contrasts in scattering-type near-field optical microscopy, Opt. Express **15**, 8550 (2007).

[27] B. Hauer, A. P. Engelhardt, and T. Taubner, Quasi-analytical model for scattering infrared near-field microscopy on layered systems, Opt. Express **20**, 13173 (2012).

[28] R. Garcia, C. J. Gomez, N. F. Martinez, S. Patil, C. Dietz, and R. Magerle, Identification of Nanoscale Dissipation Processes by Dynamic Atomic Force Microscopy, Phys. Rev. Lett. **97**, 016103 (2006).

[29] H. Choe, M.-H. Hong, Y. Seo, K. Lee, G. Kim, Y. Cho, J. Ihm, and W. Jhe, Formation, Manipulation, and Elasticity Measurement of a Nanometric Column of Water Molecules, Phys. Rev. Lett. **95**, 187801 (2005).

[30] F. Lu, M. Jin, and M. A. Belkin, Tip-enhanced infrared nanospectroscopy via molecular expansion force detection, Nat. Photonics **8**, 307 (2014).

[31] R. Garcia and E. T. Herruzo, The emergence of multifrequency force microscopy, Nat. Nanotechnol. **7**, 217 (2012).

[32] J. Jahng, B. Kim, E. S. Lee, and E. O. Potma, Quantitative analysis of sideband coupling in photoinduced force microscopy, Phys. Rev. B **94**, 195407 (2016).

[33] J. Yamanishi, Y. J. Li, Y. Naitoh, and Y. Sugawara, Nanoscale optical imaging with photoinduced force microscopy in heterodyne amplitude modulation and heterodyne frequency modulation modes, J. Photochem. Photobio. C: Photochem. Rev. **52**, 100532 (2022).

[34] J. Kischkat, S. Peters, B. Gruska, M. Semtsiv, M. Chashnikova, M. Klinkmüller, O. Fedosenko, S. Machulik, A. Aleksandrova, G. Monastyrskyi, Y. Flores, and W. T. Masselink, Mid-infrared optical properties of thin films of aluminum oxide, titanium dioxide, silicon dioxide, aluminum nitride, and silicon nitride, Appl. Opt. **51**, 6789 (2012).

[35] S. Amarie and F. Keilmann, Broadband-infrared assessment of phonon resonance in scattering-type near-field microscopy, Phys. Rev. B **83**, 045404 (2011).

[36] L. Wang, H. Wang, and X. G. Xu, Principle and applications of peak force infrared microscopy, Chem. Soc. Rev. **51**, 5268 (2022).

[37] Y.-T. Lin, H. He, H. Kaya, H. Liu, D. Ngo, N. J. Smith, J. Banerjee, A. Borhan, and S. H. Kim, Photothermal atomic force microscopy coupled with infrared spectroscopy (AFM-IR) analysis of high extinction coefficient materials: A case study with silica and silicate glasses, Anal. Chem. **94**, 5231 (2022).